Narrow-band photon beam via laser Compton scattering in an energy recovery linac

T. Akagi,[1,*] A. Kosuge,[1] S. Araki,[1] R. Hajima,[3,4] Y. Honda,[1,2] T. Miyajima,[1,2] M. Mori,[3,4] R. Nagai,[3,4] N. Nakamura,[1,2] M. Shimada,[1,2] T. Shizuma,[3,4] N. Terunuma,[1,2] and J. Urakawa[1]

[1]*High Energy Accelerator Research Organization (KEK), 1-1 Oho, Tsukuba, Ibaraki 305-0801, Japan*
[2]*SOKENDAI: The Graduate University for Advanced Studies, 1-1, Oho, Tsukuba, Ibaraki 305-0801, Japan*
[3]*Japan Atomic Energy Agency (JAEA), Tokai, Naka, Ibaraki 319-1195, Japan*
[4]*National Institutes for Quantum and Radiological Science and Technology (QST), Tokai, Naka, Ibaraki 319-1106, Japan*

(Received 30 June 2016; published 15 November 2016)

Narrow-bandwidth photon beams in the x-ray and γ-ray energy ranges are expected to be applied in various fields. An energy recovery linac (ERL)-based laser Compton scattering (LCS) source employing a laser enhancement cavity can produce a high-flux and narrow-bandwidth photon beam. We conducted the first experiment of an ERL-based LCS source in combination with a laser enhancement cavity. We obtained LCS photons with an energy of 6.95 ± 0.01 keV by colliding an electron beam of 20 MeV with a laser of 1064 nm wavelength. The photon flux at the interaction point was evaluated to be $(2.6 \pm 0.1) \times 10^7$ photons/s with an average beam current of 58 μA and an average laser power of 10 kW. The energy bandwidth was evaluated to be 0.4% (rms) with an opening angle of 0.14 mrad. The technologies demonstrated in this experiment are applicable for future ERL-based LCS sources.

DOI: 10.1103/PhysRevAccelBeams.19.114701

I. INTRODUCTION

When a relativistic electron beam collides with a laser beam, a high-energy photon beam is generated through laser Compton scattering (LCS) [1]. In a LCS source, the energy of the generated photon is adjustable by changing the collision parameters: the electron beam energy, laser wavelength, and collision angle. The LCS can generate high-energy photons with relatively low-energy electrons compared with synchrotron radiation. The energy width of the LCS photon beam can be controlled by inserting a collimator in the photon beam path because each photon has a specific energy correlated with its scattering angle. Therefore, we can obtain a narrow-bandwidth high-energy photon beam by cutting out a component of on-axis radiation with a small collimator. In addition, the generated photon inherits temporal structure and polarization from the electron and laser beams. High-energy photons from LCS sources are expected to be applied in various fields involving a wide range of photon energies ranging from keV to GeV. Examples of application fields include biomedical imaging in the keV range [2,3], the science of photo-nuclear reaction and its utilization in the nuclear industry [4,5], polarized positron production for a linear collider [6] in the MeV range, and hadron physics in the GeV range [7].

The performance of LCS sources is characterized by factors such as the photon flux, energy bandwidth, effective source size, and temporal structure. Photon flux is a common key parameter for all the applications. The energy bandwidth of the photon beam is important for observing resonant phenomena such as x-ray resonance fluorescence [8] or nuclear resonance fluorescence while maintaining a good signal-to-noise ratio. The effective source size is critical for x-ray imaging applications. Especially, in phase contrast imaging, the effective source size should be sufficiently small to obtain a clear contrast on an object's edge. To improve these parameters, various combinations of accelerators and lasers have been adopted for LCS sources.

Storage rings have been utilized for LCS sources. As a storage ring can accommodate a high-average-current electron beam, it is advantageous for realizing a high-flux photon source. Lyncean Technologies developed a compact Compton x-ray source by using an electron storage ring and a laser enhancement cavity [9], which is a high-finesse bow-tie ring cavity that stores optical pulses injected from an external mode-locked laser. The laser pulse in the cavity has a pulse energy much greater than the injection energy, and it collides with the electron beam. In HIγS at Duke University, a γ-ray photon beam was generated from the collision of electrons in a storage ring and laser photons produced by a free-electron laser (FEL). The Compton

*akagit@post.kek.jp

Published by the American Physical Society under the terms of the Creative Commons Attribution 3.0 License. Further distribution of this work must maintain attribution to the author(s) and the published article's title, journal citation, and DOI.

scattering occurred at the center of the FEL cavity. These two LCS sources are operated with different types of laser systems but are based on the same principle of accumulating laser pulses in an optical cavity for recycling the laser pulse in many beam crossings.

A linac-based LCS source for MeV γ-ray generation is under construction at the Extreme Light Infrastructure—Nuclear Physics facility (ELI-NP) to explore basic and application science by using high-brightness γ-ray beams [10]. A normal conducting linac equipped with a photo injector is used. Although the duty factor of a linac-based source is limited to $\sim 10^{-4}$, it can realize a tightly focused electron beam. Hence, it can achieve better performance than a storage-ring-based source in terms of the bandwidth, spectral density, and photon flux in a specific energy width of the γ-ray beam. A similar LCS γ-ray source is under development at the Lawrence Livermore National Laboratory (LLNL) for applications of nuclear resonance fluorescence, in which the narrow bandwidth and high spectral density are key [11–13]. Moreover, there are various operating linac-based Compton sources [14–16]. The narrow bandwidth is realized from the nature of the modern linac with a low-emittance injector. Section II describes the indispensability of the small-emittance beam to the narrow-band LCS photon beams. In this regard, linac-based LCS sources have an advantage over storage-ring-based sources, that is, the spectral density of the LCS photon beam is restricted by electron-beam heating due to quantum recoil [17].

Energy recovery linacs (ERLs) can realize a small-emittance electron beam at a high-average current. An electron beam is decelerated in the linac to recycle the beam energy before it deflects toward beam dump. Therefore, the ERL can achieve a high average current similar to that of the storage rings. They have been developed for high-power FELs and future x-ray synchrotron sources [18]. In addition, they can produce high-flux LCS photons of a narrow bandwidth. Further, ERL technology can be applied to LCS sources for any photon energy. In [19], a compact ERL-based x-ray source was proposed for biological imaging and other x-ray applications. In [20], a 350-MeV ERL was designed to generate a 2-MeV γ-ray beam for nuclear industrial applications. In these LCS sources, laser enhancement cavities were used for the high-repetition and high-density collision of electron and laser beams.

To realize future ERL-based LCS sources for x-ray and γ-ray beams, we conducted a research program to establish technologies relevant to the ERL-based LCS sources. This research was conducted using an ERL test accelerator at KEK, the compact ERL (cERL), and covered a wide range of subjects including generation and transportation of a small-emittance electron beam, design and fabrication of a high-finesse optical cavity, alignment and synchronization of electron and laser beams at collision, and management of electron beam halo to reduce radiation background downstream of the LCS beam line. In this paper, we present results these research subjects and report the first demonstration of an LCS photon beam from an ERL in combination with a laser enhancement cavity. In Sec. II, we review the physics of LCS focusing on the generation of a high-flux and narrow-band photon beam. Section III overviews the compact ERL including the LCS beamline. Section IV describes the design and performance of the laser enhancement cavity. The experimental results on LCS photon generation and demo experiments of x-ray imaging and x-ray resonance fluorescence are presented in Sec. V. We quantitatively discuss the experimental results in Sec. VI and provide conclusions in Sec. VII.

II. FLUX AND BANDWIDTH OF LCS SOURCES

This section describes the properties of LCS. Figure 1 shows the schematic of LCS, where θ is the scattering angle and ϕ $(= \pi - \theta_1)$ is the crossing angle. The energy of the scattered photon, E_x, is a function of the incident photon energy E_L, electron energy E_e, and scattering geometry [1],

$$E_x = \frac{E_L(1 - \beta\cos\theta_1)}{1 - \beta\cos\theta + (E_L/E_e)(1 - \cos\theta_2)}. \tag{1}$$

For a head-on collision, it is approximated as

$$E_x \approx \frac{4\gamma^2 E_L}{1 + (\gamma\theta)^2 + 4\gamma E_L/(mc^2)}, \tag{2}$$

where $\beta = v/c$ is the electron velocity in units of light speed, $\gamma = 1/\sqrt{1-\beta^2}$ is the Lorentz factor, and m is the electron rest mass. In the collision of an electron beam of MeV–GeV and laser of the visible and infrared light, the incident energy of photon is smaller than the electron rest mass in the electron's rest frame. Therefore, the quantum recoil is negligible and can be treated as Thomson scattering.

The energy of scattered photon is expressed as a function of the scattering angle. Therefore, we can obtain a narrow-band photon beam by cutting out an on-axis component with a small solid angle. The maximum energy of the

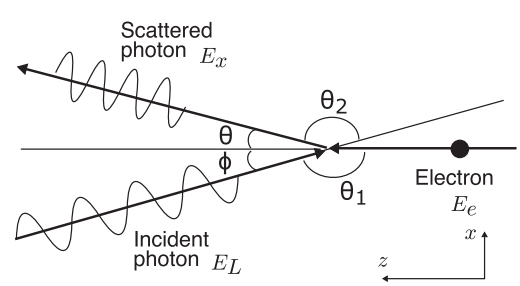

FIG. 1. Schematic of laser Compton scattering.

scattered photon is realized in the beam axis ($\theta = 0$) and is proportional to the square of beam energy as $E_x^{\max} \approx 4\gamma^2 E_L$.

The luminosity of the LCS is represented by

$$L = \frac{f N_e N_L \cos(\phi/2)}{2\pi\sigma_{ry}\sqrt{\sigma_{rx}^2\cos^2(\phi/2) + \sigma_{rz}^2\sin^2(\phi/2)}}, \quad (3)$$

and the flux is given by

$$F = \sigma_c \cdot L, \quad (4)$$

where f is the collision frequency; N_e and N_L are numbers of particles in electron and laser beam, respectively; $\sigma_{r,i}^2 = \sigma_{\mathrm{electron},i}^2 + \sigma_{\mathrm{laser},i}^2$ ($i = x, y, z$) is the convoluted spot size of the electron and laser beam at the interaction point (IP); and σ_c is the total cross section of Compton scattering and is nearly equal to the Thomson cross section $\sigma_e = 0.665 \times 10^{-28}$ m^2 with our experimental parameters. Here, z is the direction of the electron beam, and x and y are respectively the horizontal and vertical directions in the transverse plane. The electron beam collides with the laser beam in the x–z plane.

Equation (3) shows that both the electron and laser beam are required for high intensity, small beam size, and short pulse length to generate a high-flux LCS photon beam. The luminosity decreases with increasing crossing angle. The luminosity reduction due to a head-on collision ($\phi = 0$) is represented by

$$\frac{L(\phi)}{L_{\max}(0)} = \frac{\sigma_{rx}\cos(\phi/2)}{\sqrt{\sigma_{rx}^2\cos^2(\phi/2) + \sigma_{rz}^2\sin^2(\phi/2)}}. \quad (5)$$

To realize a high-flux LCS source, the crossing angle should be as small as possible. However, the crossing angle is limited because of the mechanical interference of laser mirror holders and electron beam path.

The bandwidth of scattered photons in a small angle θ is determined primarily by the collimation angle and further broadens because of the inhomogeneous natures of electron and laser beams at the collision. The relative bandwidth of scattered photons for the head-on geometry is expressed by [21]

$$\frac{\Delta E_x}{E_x} = \sqrt{(\gamma\theta)^4 + 4\left(\frac{\Delta E_e}{E_e}\right)^2 + \left(\frac{\varepsilon_n}{\sigma_e}\right)^4 + \left(\frac{\Delta\nu}{\nu}\right)^2 + \left(\frac{M^2\lambda}{4\pi\sigma_L}\right)^4}, \quad (6)$$

where $\Delta E_e/E_e$ is the energy spread of the electron beam, $\Delta\nu/\nu$ is the bandwidth of the laser photon, M^2 is the beam quality factor of the laser beam, and λ is the wavelength of the laser beam. For simplicity, we assume some symmetrical spot size of the electron beam σ_e and spot size of the laser beam σ_L on the x–y plane. The spectral broadening from the laser beam is sufficiently smaller than that from the electron beam due to the use of a narrow band laser. Therefore, the emittance and energy spread of the electron beam are dominant factors influencing the bandwidth after a small-angle collimation with $\gamma\theta \ll 1$.

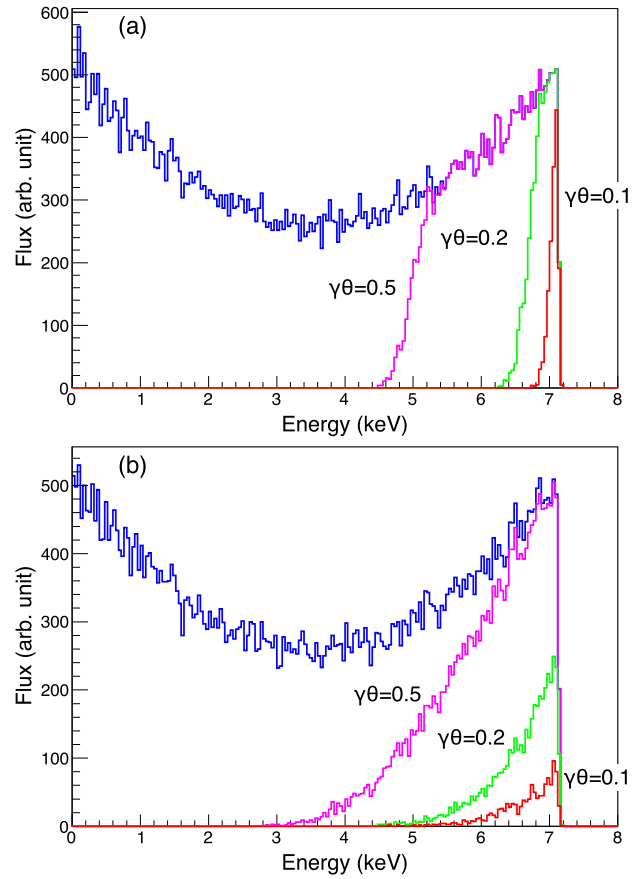

FIG. 2. Calculated LCS x-ray spectra (a) simulated with $\varepsilon_n = 1$ mm mrad and (b) $\varepsilon_n = 5$ mm mrad.

To illustrate the spectral broadening by the electron beam emittance, Monte Carlo simulations of LCS with typical parameter sets are shown below. Figure 2 shows examples of LCS x-ray spectra calculated using a Monte Carlo code, CAIN [22], where the electron energy $E_e = 20$ MeV, electron beam size $\sigma_e = 30\ \mu$m, laser beam size $\sigma_L = 30\ \mu$m, rms relative energy spread of the electron beam is $\Delta E_e/E_e = 0.1\%$, rms relative bandwidth of the laser beam is $\Delta\nu/\nu = 0.006\%$, and the crossing angle $\phi = 0$ (head-on collision). Figure 2 shows LCS spectra for two cases of normalized emittance: (a) $\varepsilon_n = 1$ mm mrad and (b) $\varepsilon_n = 5$ mm mrad. The width of the calculated spectrum increases with increasing electron beam emittance, even if we choose a small collimation angle. In case (a), the spectral broadening due to the normalized emittance, $(\varepsilon_n/\sigma_e)^2 \sim 0.1\%$, is smaller than the bandwidth determined by the collimation angle, even for small-angle collimation ($\gamma\theta = 0.1$). To obtain a narrow-bandwidth photon, a small-emittance electron beam is necessary.

The requirements for a high-flux and narrow-bandwidth Compton source are summarized as follows. The accelerator requires high current, low emittance, and small energy spread, and the laser system requires high power, small spot size, and small bandwidth. An ERL with a laser enhancement cavity satisfies these requirements.

III. ACCELERATOR

A. Compact ERL

The cERL is a test facility constructed for the development of accelerator components and technologies necessary for future ERL-based light sources such as diffraction-limited x-ray synchrotron sources, high-flux laser Compton x-ray/γ-ray sources, and high-power FELs [18]. In the design and construction of the cERL, we primarily focused on the generation and acceleration of a small-emittance electron beam with a high repetition rate, that is, high average current. The research and development at the cERL include the following: a photo-cathode DC electron gun [23], superconducting accelerators for the injector [24] and the main linac [25], transportation of a small-emittance electron beam [26], and diagnostics and instrumentation for a high average current beam. A detailed description of the design and construction of the cERL is given in [27]; we briefly introduce accelerator components relevant to the LCS experiment in this section.

Figure 3 shows the layout of the cERL, which consists of an injector, a superconducting linac, and a recirculation loop. A collision chamber for the LCS is located in the long straight section of the recirculation loop. In the LCS experiment, the cERL is operated at an injection energy of 2.9 MeV, recirculation energy of 20 MeV, and pulse repetition rate of 162.5 MHz. In this paper, energy represents the total energy. In the experiment, the beam current was limited to 0.1 mA: the value approved by the regulatory authority at that time.

The injector is equipped with a photo-cathode DC gun and cryomodule to accommodate superconducting cavities (2-cell $\times$ 3-cavities) operated at 1.3 GHz. The electron beam from the injector is merged with the recirculating beam by using the injection chicane. It is known that the dilution of electron beam emittance due to space charge force and a time-varying rf field can be sufficiently compensated for with an optimum design of the injector [28,29]. We conducted a computational optimization based on a multiobjective genetic algorithm to determine the injector parameters under geometrical and physical constraints. The tuning parameters are the strength of two solenoid and five quadrupole magnets, amplitude and phase of a 1.3 GHz buncher cavity, and three injector cavities. Figure 4 shows the emittance, transverse beam size, and bunch length along the injector after the optimization for an electron bunch of 0.77 pC. The designed electron beam parameters after the main linac are as follows: electron beam energy of 20 MeV, normalized rms emittance of 0.26/0.24 mm-mrad (horizontal/vertical), energy spread of 5.9 keV (rms), and bunch length of 2.9 ps (rms).

Unwanted beam loss is a critical concern in the operation of ERLs because the radiation dose and local heat deposit produced by a small but continuous beam loss may cause problems in radiation safety and machine protection. Hence, understanding the mechanism of beam loss and planning strategies to reduce beam loss are some of the important research subjects in the cERL. Therefore, we installed movable collimators to scrape off the beam halo and localize radiation dose. Each collimator consists of four copper plates: two each for the horizontal and vertical planes. The locations of the collimators are shown in Fig. 3. In daily operations of the cERL, we scrape off the beam halo by inserting the collimators close to the beam axis so that the beam core does not hit the collimators.

In the LCS experiment, the beam loss around the IP produces streaming radiation overlapping with the Compton-scattered photon beam. Such streaming radiation often degrades the quality of the experimental data obtained using Compton-scattered photon beams. Therefore, we carefully managed the beam loss around the IP.

The IP for the LCS is located before the second arc of the recirculation loop. This position has been chosen so that beam tuning for a small spot size at the collision is ensured and the extraction of Compton-scattered photons is possible through the gap of the first bending magnet in the second arc. The collision section is configured as a set of quadrupole magnets symmetric to the IP. The set of quadrupole magnets enables us to control the beam size in both the horizontal and vertical directions at the IP independently without affecting the beam optics in the other section of the recirculation loop.

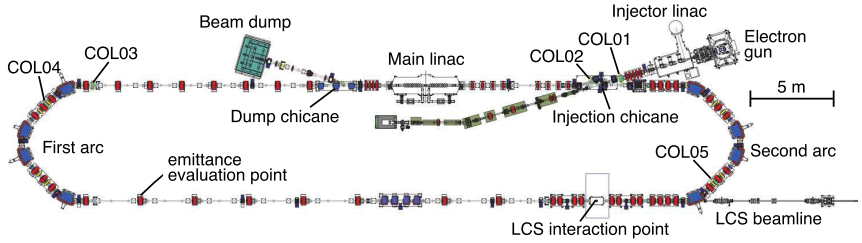

FIG. 3. Layout of the Compact ERL. COL1-COL5 are movable collimators to scrape off the beam halo.

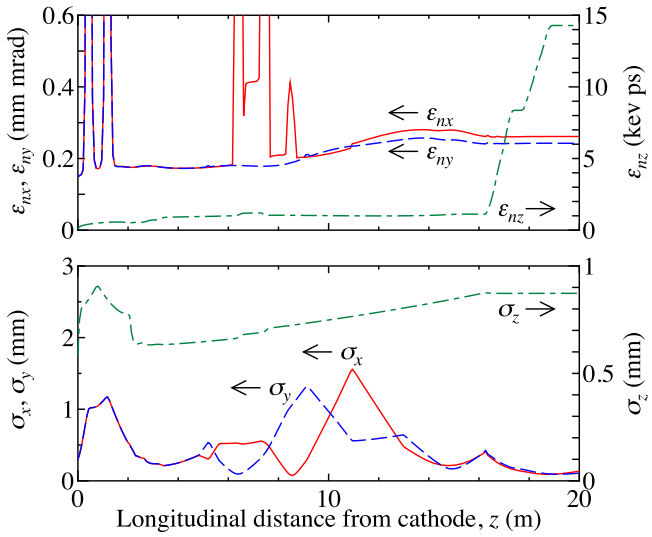

FIG. 4. Beam evolution in the injector optimized for 0.77 pC bunch charge: normalized rms emittances (top), transverse beam sizes and bunch length (bottom) versus position in the injector.

As discussed in the previous section, the collision luminosity is a function of the spot size of both the electron and laser beams. As the luminosity for a collinear collision with round Gaussian beams is inversely proportional to $\sigma^2_{\mathrm{electron}} + \sigma^2_{\mathrm{laser}}$, a small size of the electron beam is preferable for an efficient collision. In a collision at a finite crossing angle, focusing an electron beam perpendicular to the crossing plane is more efficient, as shown in Eq. (3). We designed the final focusing magnets so that we can control the horizontal and vertical sizes of an electron beam at the collision independently. However, a small electron beam size at the collision is unfavorable because of beam loss and x-ray bandwidth. The tight

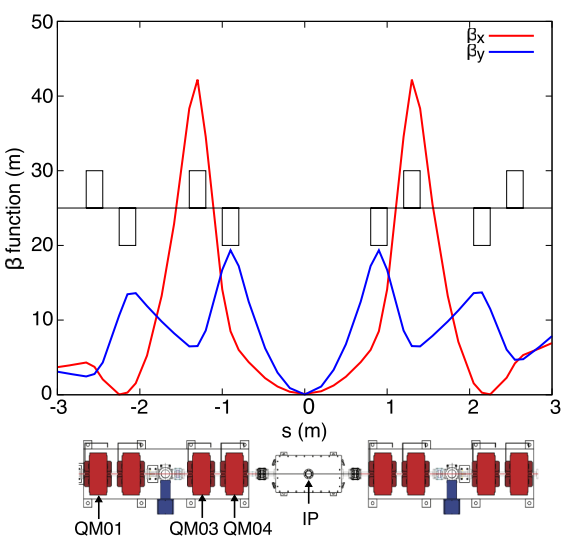

FIG. 5. Beam envelopes designed to obtain a tight focused electron beam at the IP, $\beta_x^* = 0.11$ m and $\beta_y^* = 0.037$ m.

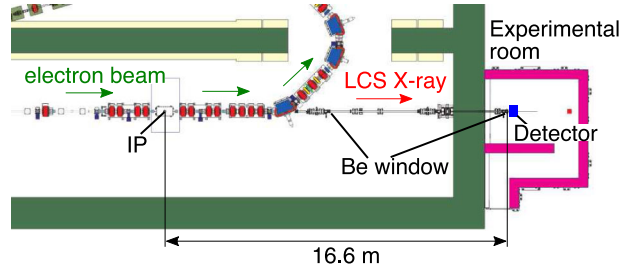

FIG. 6. Schematic drawing of the LCS beam line.

focusing at the IP results in a large betatron amplitude at the final focusing quadrupole, which can be a beam loss point. The experimental room for the Compton scattered photon beam is located outside the accelerator shield. The distance from the IP to the experimental area is approximately 16 m. With this long beam path, we were able to obtain narrow-bandwidth x-rays by selecting an on-axis part of the photon beam, as shown in Sec. V. In the experiment, we rely on an electron-beam tuning strategy of focusing the electron beam down to a spot size comparable to the laser beam size at the collision. In addition, the horizontal beam size is focused looser than the vertical beam because the laser beam has a horizontal crossing angle, as explained in the following section, and the luminosity is insensitive to the horizontal beam size. Figure 5 shows a beam envelope designed to obtain the betatron function at the IP; $\beta_x^* = 0.11$ m and $\beta_y^* = 0.037$ m.

B. LCS beam line

The LCS x-rays were transported to an experimental room through a vacuum tube called the LCS beam line. Figure 6 shows the layout of the LCS beam line. As the expected energy of an LCS photon is approximately 7 keV, the LCS beam line should be evacuated to avoid attenuation in air. Two beryllium windows were installed at both ends of the LCS beam line. The thicknesses of beryllium windows located at the accelerator and the experimental room sides are 0.25 and 0.3 mm, respectively. A collimator with a diameter of 24 mm is located 6.3 m away from the IP to reduce the background. An x-ray detector, that is, a silicon drift detector (SDD), was located 16.6 m away from the IP and was used for evaluating the LCS photon flux. The detector has an aperture with a diameter of 4.66 mm, and the source-detector opening angle is 0.14 mrad.

IV. LASER SYSTEM

The laser system is the key of the LCS photon source. To produce a high-flux x-ray, a high-power and tightly focused laser pulse with a repetition rate that matches the electron beam is needed. We have developed an optical cavity for the LCS IP, in which laser pulses from a mode-locked laser are stacked and enhanced by several orders of magnitude. Considering the technical maturity of mode-locked lasers

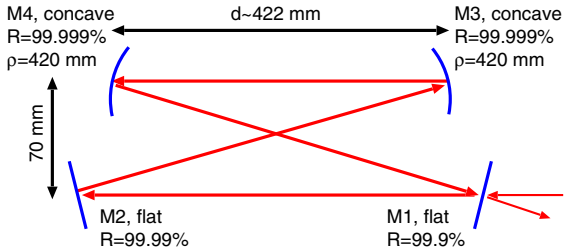

FIG. 7. Schematic of the bow-tie 4-mirror cavity.

oscillator and low-loss cavity mirrors, we chose a Nd-based laser system of 1064 nm wavelength. The laser pulse width is 5.65 ps (rms).

The laser system consists of the laser oscillator and its transfer optics, the feedback control system, and the optical cavity and its vacuum chamber.

A. Cavity design

The optical cavity should realize a small spot size at the IP with keeping the round-trip length matched to the beam repetition rate. A 4-mirror bow-tie ring cavity with two concave mirrors and two flat mirrors is suitable for this purpose [30]. Figure 7 shows the schematic of the 4-mirror cavity. The cavity realizes a small spot size at a location between the two concave mirrors, M3 and M4, and a collimated beam exists in the region outside these mirrors. The spot size can be controlled by the distance between the concave mirrors (d), and the radius of curvature of the mirrors (ρ) is fixed. The round-trip length can be independently controlled by shifting the flat mirrors, M1 and M2. Table I summarizes the design parameters of the optical cavity.

By considering the practical constraints such as the space for installation, we set the round-trip length to be 1845 mm, which corresponds to a repetition rate of 162.5 MHz and 1/8 sub-harmonics of the cERL's RF. Figure 8 presents the photograph of the optical cavity structure. Two sets of 4-mirror cavities having a common focal point are combined symmetrically in the same structure. In the present study, only one set was used for the experiment, and a two-set operation will be conducted in a future study to simultaneously produce two x-ray beams (for example; polarization, energy). The planes of the 4-mirror cavities are vertically placed in the structure, considering easy manual access in the vacuum chamber. The electron beam

TABLE I. Design parameters of the optical cavity.

Repetition rate	162.5 MHz
Finesse	5600
Spot size at the IP (σ_x/σ_y)	20/30 μm
Input angle of mirrors	4.3°
Diameter of mirrors	25.4 mm
Curvature radius of mirrors	420 mm

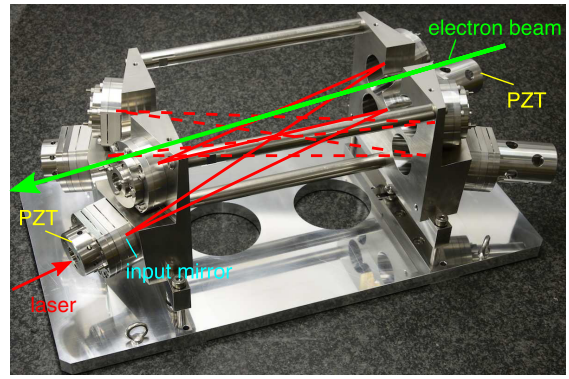

FIG. 8. The optical cavity structure.

passes the center (the beam duct is not shown) with a crossing angle of 18°.

The flat and concave mirrors were provided by REO (Research Electro-Optics, Inc.) and LMA (Laboratoire des Matériaux Avancés), respectively. These mirrors are dielectric multilayers coated on super-polished substrates made of fused silica. The diameter and thickness are 25.4 and 6.2 mm, respectively. The radius of curvature of the concave mirrors is 420 mm. As shown in Fig. 7, the reflectance of the coupling mirror M1 is 99.9%, and the reflectances of M2, M3, and M4 are 99.99%, 99.999%, and 99.999%, respectively. As the reflectance of M1 was designed to be much lower than that of the other mirrors, the loss on M1 dominates the total loss of the cavity. According to the suppliers' data sheet, the finesse and enhancement factor of the optical cavity were calculated to be 5600 and 2200, respectively. The laser pulse width is limited by the dispersion of the mirrors when the pulse width is less than 100 fs or finesse is more than 10000. In our experimental condition, it is not so serious, because we store a laser pulse of 5.65 ps (rms) in the cavity with finesse of 5600.

The transverse mode of the laser beam in the cavity is mostly defined by $d-\rho$, that is, the difference of distance between the concave mirrors and their corresponding radius of curvature. Figure 9 shows the calculated dependence. As $d-\rho$ approaches zero, the spot size at the IP can be smaller, while the cavity moves closer to the stability edge. As the finite input angle $\alpha = 4.3°$ on the concave mirror changes the effective focal length (f_s, f_t) in the two planes, the transverse mode becomes astigmatic, that is, the transverse profile is an ellipse. f_s and f_t are expressed as [31]

$$f_s = \frac{\rho}{2\cos\alpha}, \tag{7}$$

$$f_t = \frac{\rho}{2}\cos\alpha, \tag{8}$$

where f_s and f_t are the effective focal lengths in the sagittal plane (horizontal) and tangential plane (vertical) of the cavity, respectively. The designed spot sizes (rms) at the IP

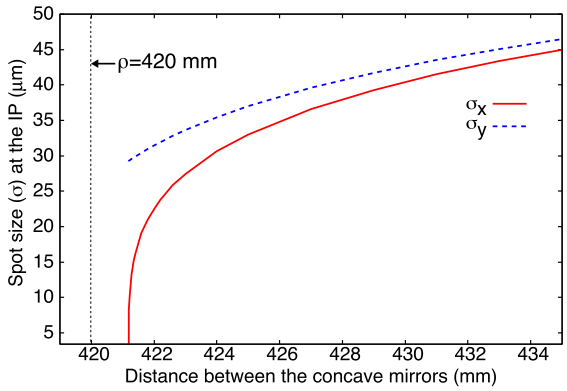

FIG. 9. Dependence of the spot size at the IP on distance between the concave mirrors.

are 20 μm on the horizontal plane and 30 μm on the vertical plane. Figure 10 shows the calculation of the spot sizes of the laser beam along the propagation direction in the cavity.

To control the round-trip length of the cavity precisely, piezo actuators are implemented in the mirror holders of M1 and M2. The positions of the mirrors M3 and M4 are fixed to remain the spot size. Each piezo actuator is supported by a leaf-spring structure, and it pushes the mirror from behind to shift the mirror position longitudinally. We designed two piezo actuators with lengths 70 and 15 mm for different strokes.

The longer actuator has a stroke of approximately 20 μm, corresponding to a repetition rate of approximately 2 kHz. This is used to compensate for a slow but large variation of the cavity length. In contrast, the short actuator has a stroke of approximately 5 μm. The shorter stroke is intended for reducing sensitivity to electrical noise. It is used for fast control of the cavity length for synchronizing the laser pulse with the accelerator. The timing jitter should be less than 1 ps (rms) to avoid luminosity reduction. In addition, for suppressing the thermal expansion, temperature changes of the optical cavity should be less than 1 °C. The change in the cavity length with 1 °C rise in temperature is more than 20 μm because the thermal expansion

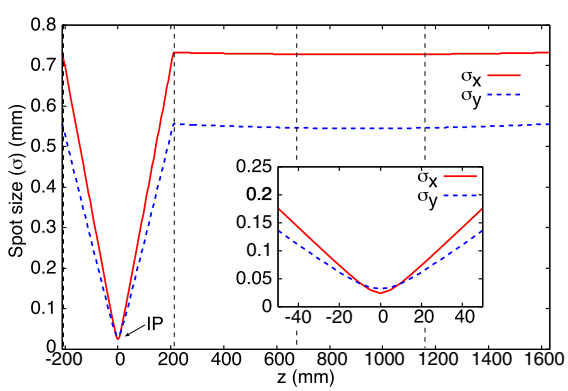

FIG. 10. Spot size of laser beam along the propagation in the cavity. Vertical dotted lines show the position of the mirrors.

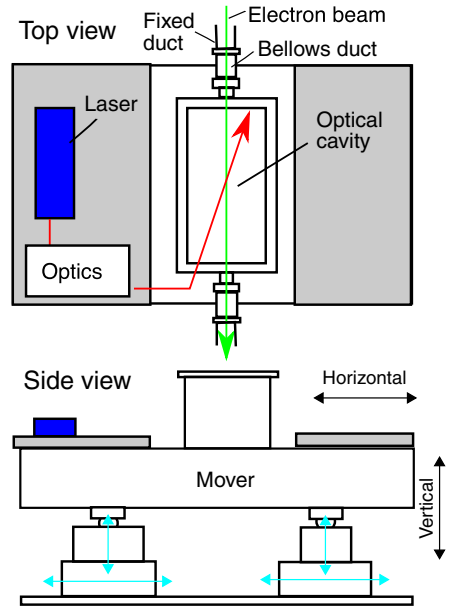

FIG. 11. Schematic drawing of the cavity system. The whole optical system was mounted on a mover, an optical bench movable in the two transverse directions of the electron beam.

coefficient of SUS304 is 17.3×10^{-6}/°C. Note that 20 μm is a stroke of the long piezo actuator of the cavity, and the optical cavity is made of SUS304.

B. Mover and transfer optics

Figure 11 shows the setup of the cavity system. The optical cavity structure is installed in a vacuum chamber connected to the beam duct of the accelerator. The entire optical system is mounted on a mover, which is an optical bench movable in the two transverse directions of the electron beam. The chamber is connected to the fixed beam duct at both ends with a bellows duct. The mover enabled us to precisely adjust the spatial overlap between the two beams without affecting the electron beam.

Figure 12 shows the schematic inner structure of the vacuum chamber. To avoid electromagnetic effect on

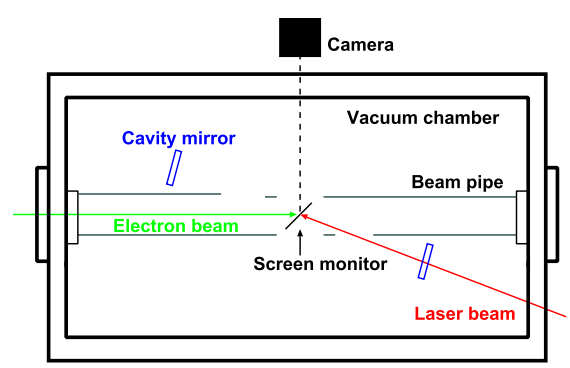

FIG. 12. Schematic figure of the inner layout of the vacuum chamber. A removable screen monitor was located at the IP.

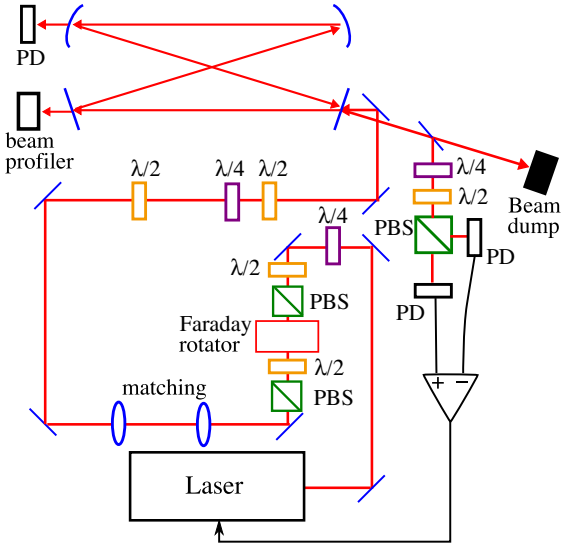

FIG. 13. Setup of the optical system. $\lambda/2$: half-wave plate, $\lambda/4$: quarter-wave plate, PBS: polarizing beam splitter, PD: photodiode, isolator consists of Faraday rotator and PBS.

the short bunched electron beam due to electrical discontinuities of the beam duct, a shielding beam pipe is placed in the cavity structure. This beam pipe has apertures of 10 mm × 40 mm at the horizontal sides for transmitting the laser beam. The designed rms sizes of the laser spot are $\sigma_x = 0.3$ mm and $\sigma_y = 0.2$ mm at the aperture, with a clearance of 20-σ. The diffraction loss due to the aperture was estimated to be negligible.

For monitoring the electron and laser beams at the IP, a screen monitor is installed. The beam pipe has a 20 mm aperture on the top for inserting the screen and an aperture on the side to view the screen through a view port by using a camera.

Figure 13 displays the optical system. A commercial laser system consisting of a mode-locked oscillator and an amplifier (ARGOS, TimeBandwidthProduct) is used. The oscillator is custom modified to allow us to control a piezo actuator attached to one of the mirrors in the oscillator. This was used for locking the cavity resonance.

After inserting an isolator, a lens pair was installed to match the laser beam to the eigenmode of the cavity. The polarization of the laser was adjusted using wave plates. Next, it was injected to the cavity from a view port of the vacuum chamber. The laser power at the exit of the amplifier was 30 W, and decreased to 24 W because of loss in the transfer optics. The beam reflected from the cavity was transported to a water-cooled dump. Moreover, a part of the reflected beam was sampled and used for the feedback system of the cavity.

C. Feedback system

Two conditions require feedback control: the first to maintain the high-finesse optical cavity on the resonance condition, called cavity locking: the other to synchronize the laser pulse in the cavity with the electron beam, called phase locking. Figure 14 shows the block diagram of the feedback system. The cavity locking was performed with the piezo actuator inside the oscillator. The phase locking was performed with the piezo actuator of the cavity. As cavity locking requires a faster control for maintaining a narrow resonance condition, a faster knob, that is, the oscillator piezo is used.

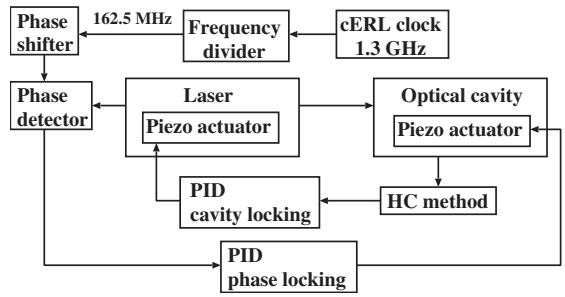

FIG. 14. Block diagram of the feedback system.

The timing synchronization is achieved by adjusting the length of the optical cavity. The error signal for phase locking was produced by mixing two signals: the accelerator rf signal and the signal from a photodiode inside the laser oscillator. This error signal has the information about the frequency and phase difference between two input signals.

The error signal for cavity locking was produced through the polarization-sensitive detection of the reflected beam. This is a variation of the Hänsch-Couillaud method [32]. As the cavity is slightly polarization-dependent because of the finite input angle on the mirrors, the reflected beam changes the polarization when it crosses a resonance peak [33]. After adjusting the polarization with two wave plates, the reflected beam is split by using a polarizing beam splitter and detected using two photo detectors. The signals from the two detectors are fed into a differential amplifier, and the output could be used as an error signal.

Figure 15 shows a typical error signal with the cavity transmission, the peak height of which is proportional to the stored laser power. This figure is obtained by scanning the resonance condition of the cavity. The error signal crosses zero at the resonance peaks. By processing the error signal through proportional-integration-differential (PID) control electronics, the control signal of the piezo actuator was produced. Two peaks in the transmission corresponded to the resonance conditions of the two linear polarizations. The polarization of the injected beam was adjusted to be dominated by one polarization component while containing a small amount of the other component. The difference between peak heights showed the power balance of the two components. This unbalanced beam was intended for

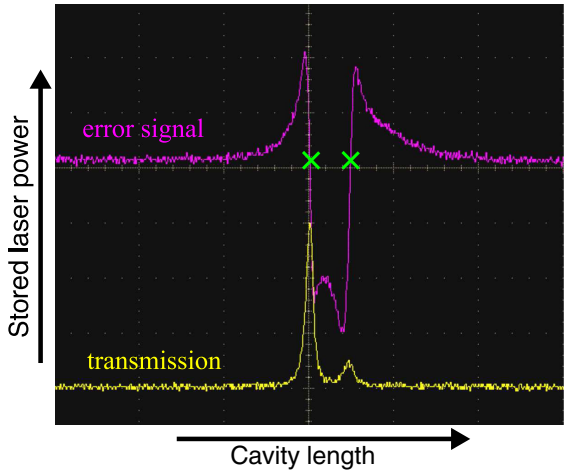

FIG. 15. The intensity of the transmitted light and the error signal.

efficiently resonating the laser power in one polarization, producing a clear error signal.

D. Performance

As the beam size at the collimated region in the optical cavity reflects the spot size at the focal point, we were able to estimate it by measuring the size of the beam transmitted through M2. Figure 16 shows the profile measured behind M2 when scanning the cavity length. The sizes of the transmitted beam were measured to be $\sigma_x = 0.73$ mm and $\sigma_y = 0.61$ mm. The spot sizes at the focal point were calculated to be $\sigma_x = 24 \pm 1$ μm and $\sigma_y = 32 \pm 1$ μm.

By scanning the cavity length in a wide range, we were able to observe many resonance peaks separated by a distance of the wavelength. Figure 17 shows an example of resonance peaks. The peak heights represent the power resonating at each peak. The highest peak corresponds to the cavity length that perfectly matches the repetition rate of the mode-locked laser. In addition, the highest peak is the most efficient for storing the power but has

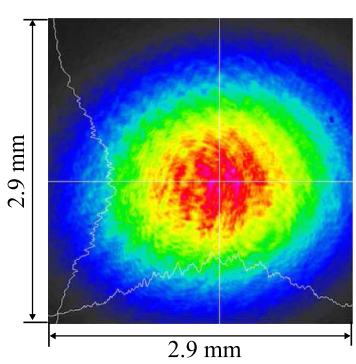

FIG. 16. Laser beam profile measured at behind M2. A regular fringe structure is due to neutral density filters for the laser beam profiler.

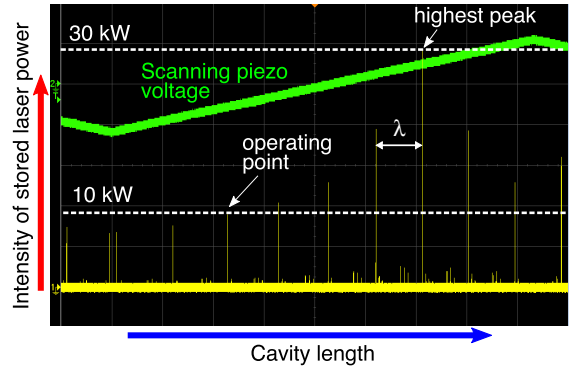

FIG. 17. Observation of resonance peaks.

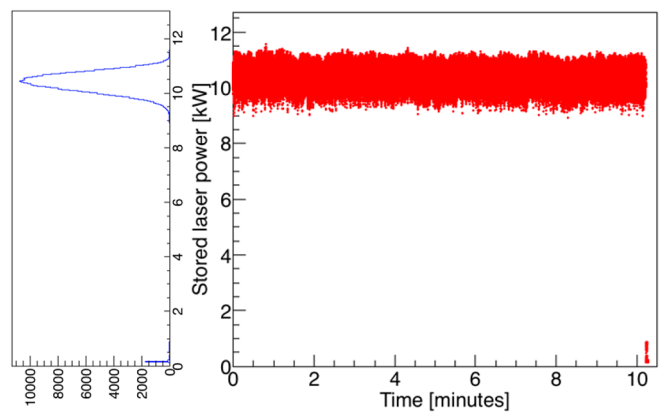

FIG. 18. Stability of the stored laser power in the optical cavity.

the narrowest width, being sensitive to disturbance. The resonance width increases as the height decreases. Although the enhancement gain is reduced, the lower peak is beneficial in terms of stability for keeping the cavity at resonance. For our first experiment, we have chosen the peak shown in Fig. 17, which is the fifth peak from the highest, to maintain stability at resonance. Note that the peak lowering implies spectrum narrowing, which

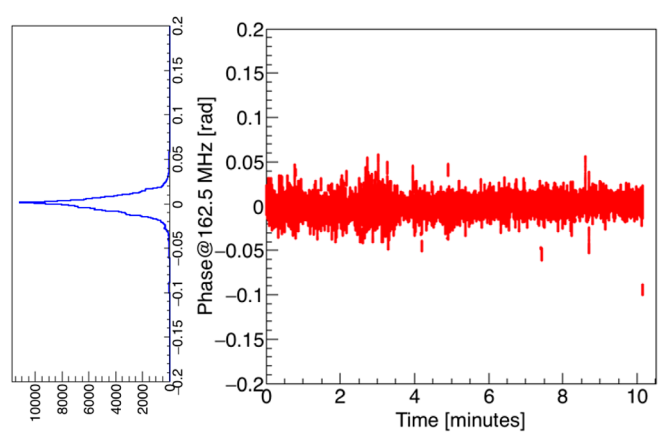

FIG. 19. Stability of the laser phase in phase locking feedback.

TABLE II. Parameters of the laser in the optical cavity at the LCS experiment.

Wavelength	1064 nm
Pulse energy	61.5 μJ
Injected pulse width (rms)	5.65 ps
Stored pulse width (rms)	10 ps
Repetition rate	162.5 MHz
Collision angle	18°
Spot size at the IP (σ_x/σ_y)	24/32 μm
Spot size on mirrors (σ_x/σ_y)	0.7/0.6 mm

may result in pulse-width broadening in the cavity. The stored pulse width was estimated to be approximately 10 ps (rms) for the fifth peak.

The laser power stored in the optical cavity was estimated from the transmitted power. The transmittance of the mirror M3 was independently measured to be 5 ± 1 ppm in advance. Figure 18 shows a typical stored power variation in the optical cavity. The average laser power is 10.4 kW with an rms fluctuation of 0.3 kW. The power enhancement factor of the optical cavity was estimated to be 430 with an input power of 24 W. This enhancement factor is lower than the original design value because we chose the lower resonance peak.

The timing stability between the laser pulse and electron bunch was monitored using a phase detector used for the phase-locking feedback. Figure 19 shows the statistical variation of the phase. The width of the distribution is 9.96 mrad, which corresponds to an rms of 9.75 ps. The phase variation is somewhat greater than the electron bunch length, 2 ps, and the injected laser pulse width, 5.65 ps. The effects of the laser phase variation on the LCS photon generation are discussed in Sec. VI.

Table II summarizes the laser parameters.

V. EXPERIMENT

A. Alignment and focusing of electron beam

We confirmed the alignment and focusing of the electron beam at the IP before the LCS experiment. Although the usual operation and LCS x-ray generation experiment of the cERL were performed in the CW mode, the beam tuning was performed in the burst mode, which cut out a bunch train of 1 μs duration at 5 Hz. The burst mode allowed us to destructively measure the beam by using screen monitors. We first examined the beam alignment and then optimized the beam focusing at the IP.

The electron beam alignment at the IP is necessary to precisely set the x-ray detector on the LCS beam path. As the detector is prealigned with respect to the quadrupole magnets of the LCS section, the electron beam should be aligned with reference to the magnets. The alignment was conducted using a beam-based technique to set the beam path on the field center of the nearest quadrupole magnets

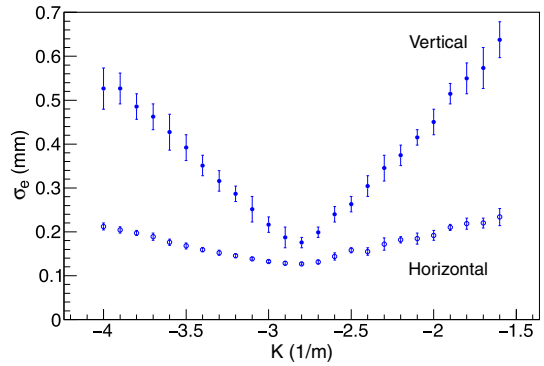

FIG. 20. Tuning of the electron beam sizes by the Q-scan using screen monitor at the IP.

at both sides of the IP. We evaluate that the angle of the electron beam path can be aligned within 0.2 mrad accuracy from the resolution of the screen monitors and the installation error of the quadrupole magnets.

After the beam alignment was completed, we tuned the electron beam focusing at the IP. To realize an efficient collision, we designed electron beam optics so that the horizontal and vertical envelopes have waists at the IP simultaneously. As the strongly focused optics was sensitive to errors, an *in-situ* adjustment was necessary. The screen monitor at the IP was used to check the beam directly. We employed quadrupole magnets, QM01-QM04 as shown in Fig. 5, to obtain optimum focusing at the IP. As shown in Fig. 20, we scanned the strength of the quadrupole magnet QM04 while measuring the beam sizes at the IP. The strength of the quadrupole magnet, K-value, was assumed to be proportional to the excitation current of the magnet. A fine adjustment of another quadrupole magnet, QM03, was needed to realize the waists of both planes at the same setting of magnets.

Although a smaller IP size is better from the viewpoint of luminosity, beam optics practically limited because of due to beam loss. A smaller spot size increased the beam divergence, resulting in a larger beam size at the location of the quadrupole magnets, QM03 and QM05. We observed an uncontrollable transverse beam halo, which could hit the beam duct at such locations of large beams. To solve this problem, we adjusted the beam size at the IP so that it does not become too small by using an upstream quadrupole magnet, QM01.

As the electron beam size at the IP was smaller than the resolution of the screen monitor, the size was indirectly estimated from the electron beam emittance and beta function. First, the beam emittance was measured using the Q-scan method at the straight section upstream of the collision optics, where the beam focusing was weaker and the minimum beam size in the Q-scan method was larger than the resolution of the screen monitor. Figure 21 shows the measurement of beam size (σ_e) when scanning the strength of a quadrupole magnet. This measurement has

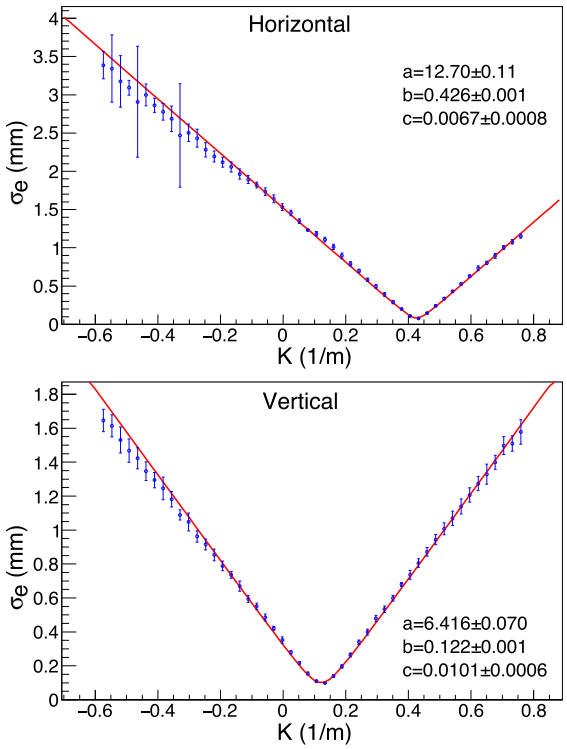

FIG. 21. Measurement of emittance with LCS operation mode. The red line is the fitted curve with a parabolic function.

been performed using a bunch charge of 0.44 pC. Although the bunch charge in the LCS experiment described as follows is not exactly the same, we assume that the effects on the emittance is sufficiently small by evaluating space charge effects.

By fitting these data with a parabolic function, $\sigma_e = \sqrt{a(k-b)^2 + c}$, leaving a, b, and c as free parameters, the normalized emittance can be obtained by $\varepsilon_n = \gamma\beta\sqrt{ac}/L_1^2$, where k is the K-value defined previously and $\gamma\beta = 39.1$ for the beam energy. L_1 (= 6.01 m) is the distance between the center of the quadrupole magnet and screen monitor. The results for each plane are $\varepsilon_{nx} = 0.32 \pm 0.02$ mm mrad and $\varepsilon_{ny} = 0.28 \pm 0.01$ mm mrad.

Second, beta functions at the IP were estimated from the data in Fig. 20. Even if the actual beam size at some data points is smaller than the resolution of the screen monitor and not measured directly, the slopes reflect the beta function, assuming linear optics. By fitting these data with a linear function $\sigma_e = Ak + B$, the average of both slopes for each plane are $A_x = (0.085 \pm 0.008) \times 10^{-3}$ m^2 and $A_y = (0.36 \pm 0.03) \times 10^{-3}$ m^2. In combination with the emittance, which is measured separately, the beam size at the IP can be estimated by $\sigma_0 = \varepsilon_n L_2^2/(\gamma\beta A)$, where $L_2 = 0.9$ m is the distance between the center of QM04 and the screen monitor at the IP. The beam sizes at the IP are determined to be $\sigma_x = 78 \pm 9$ μm and $\sigma_y = 16 \pm 2$ μm for the horizontal and vertical planes, respectively.

TABLE III. Parameters of the electron beam at the LCS experiment.

Energy	20 MeV
Bunch charge	0.355 pC
Bunch length (rms)	2 ps
Spot size (σ_x/σ_y)	78/16 μm
Emittance ($\varepsilon_{nx}/\varepsilon_{ny}$)	0.32/0.28 mm mrad
Repetition Rate	162.5 MHz

Table III lists the. parameters of the electron beam.

B. Position and timing adjustment of laser beam

To optimize the collision condition of laser pulses and electron bunches, spatial and temporal overlap must be established. We first established the spatial overlap of the laser pulses and the electron bunches at the IP, and then optimized temporal overlap.

At first, the spatial overlap was adjusted, leaving the temporal synchronization unlocked. For the initial adjustment, the screen monitor at the IP was used. As described in Sec. IV, this monitor enables us to directly check the position of both beams. Figure 22 shows an example of beam position measurement at the IP screen. As the entire

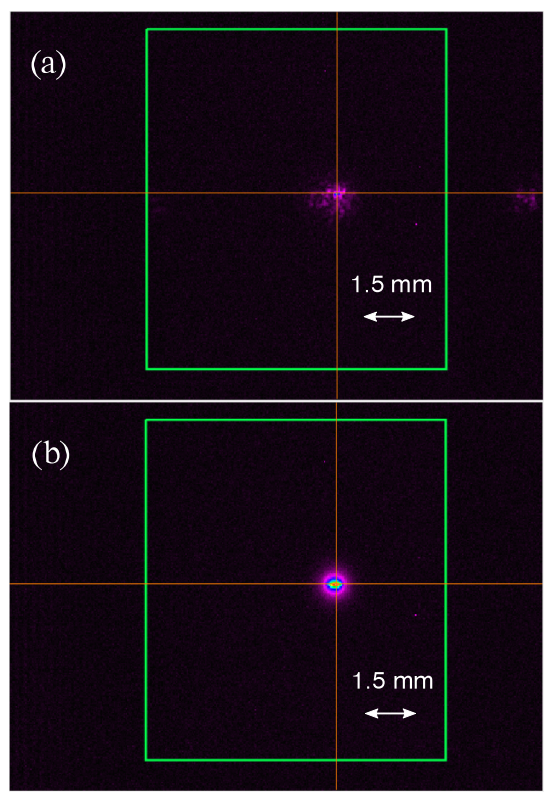

FIG. 22. Snapshots of the screen monitor located at the IP. (a) shows the laser profile without an electron beam. (b) shows the electron beam profile.

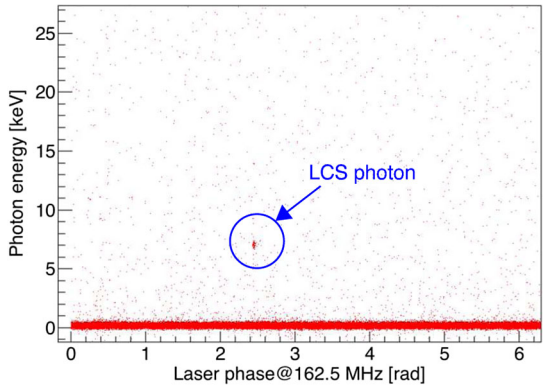

FIG. 23. Detected energy versus phase difference between the cERL rf and laser.

laser system including the screen monitor is mounted on the mover, we can move the laser system so that the electron and laser beams stay at the same position on the screen. By considering the resolution of the screen monitor to distinguish the center of the spot position, we could set the spatial overlap within 0.1 mm accuracy.

Next, we observed x-ray signals by using the SDD in the experimental room. Figure 23 plots the detected energy versus phase difference between the cERL rf and laser. As the trigger of the detection was random and the timing synchronization was unlocked, implying that the timing between the laser pulse and electron bunch was random, most events were detected to have zero energy. The temporal overlap of the electron and laser pulses was realized at a specific laser phase, where a cluster of events can be observed at the expected x-ray energy of 6.9 keV. The mover position was finely adjusted after determining the LCS signal. Figure 24 (top) illustrates the dependence of the LCS signal rate on the vertical scanning of the mover position. The rms width of the distribution is approximately 30 ± 3 μm. It is almost consistent with the convolution of the laser and electron beam sizes in the vertical direction.

Next, the timing synchronization system was turned on to lock the laser phase to the electron beam. The laser phase can be controlled using a phase shifter in the reference line from the cERL, as described in Fig. 14. Figure 24 (bottom) illustrates the dependence of the LCS signal rate on the laser phase. The width of the distribution is 13.4 mrad, which corresponds to 13 ps (rms). This is almost consistent with the convolution of the stored laser pulse width and laser phase jitter.

C. X-ray flux and spectrum

Figure 25 shows the energy spectrum detected using the SDD. The energy scale of the detector was calibrated using 5.89 and 6.49 keV x-rays of a Fe-55 checking source. The central energy and energy width of the LCS signal were measured to be 6.95 ± 0.01 keV and 78.1 ± 0.2 eV in rms respectively, as raw data. The energy resolution of the detector was estimated to be 72 eV at 6.95 keV in rms from

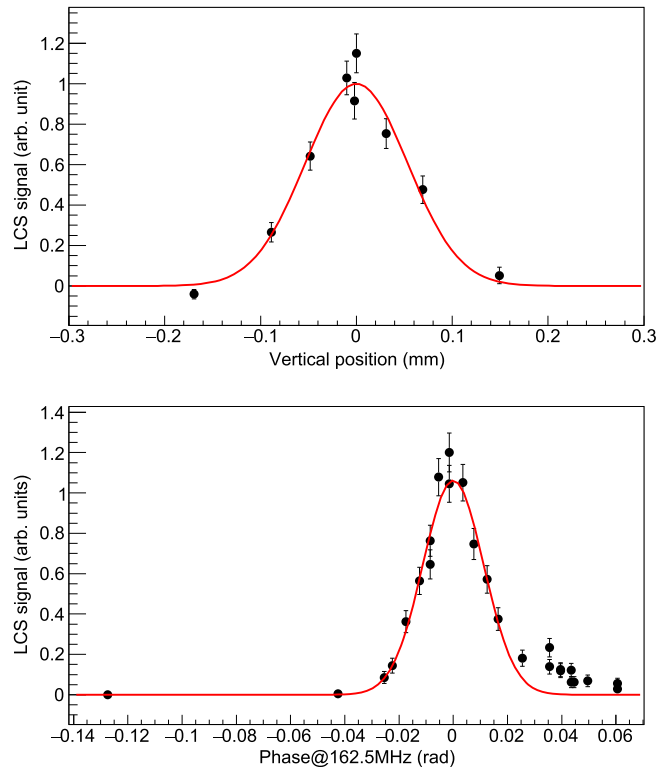

FIG. 24. LCS signal rate as a function of the vertical position of the laser beam (top) and timing of laser phase (bottom).

the peak width in the calibration. The measured peak width mostly originated from the detector's resolution. We estimated the actual spectrum width to be 30 ± 2 eV by subtracting the contribution of the detector's resolution. The LCS signal rate was measured to be 1370 count/s with the detector.

D. Demonstration of x-ray imaging

We conducted a demonstration experiment of x-ray imaging. The setup is shown in Fig. 26. A sample is placed behind a beryllium window in the experimental room. After a 2.5 m long drift space filled with He, called the He-path, a two-dimensional x-ray detector (HyPix-3000, Rigaku) is placed. Its active area is 77.5×38.5 mm^2, and the spatial resolution, corresponding to the pixel size, is 100 μm. The He-path is included for reducing the effect of x-ray absorption. For 7 keV x-rays, the transmittance was calculated to be only 1.3% with 2.5 m of air. It could be improved to 27% if 70% of air is replaced by He gas.

Figure 27 shows an example of an image of a hornet. The structures in the wings and edges of the body can be clearly seen. Owing to the drift space between the sample and detector, x-ray refraction resulted in a refraction contrast image on the detector.

Figure 28 shows the stability of x-ray flux during image acquisition. The signal rate at a blank area in the image was used to calculate the flux. The linear decrease of the count

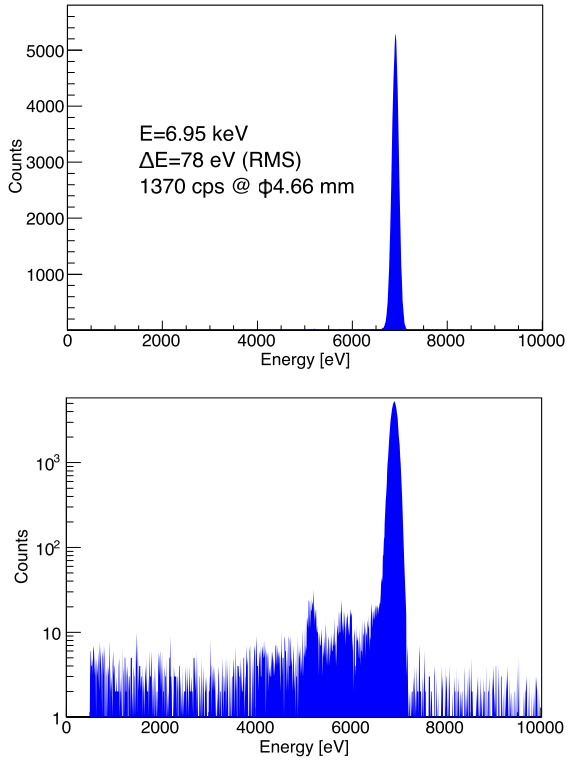

FIG. 25. Energy spectrum of the observed LCS photons with a linear scale (top) and a logarithmic scale (bottom).

rate is attributed to a constant leak of He gas from the He-path. This result shows the realization of a stable laser-beam collision with a small spot size. Typically, it took 8 min to obtain an image of the hornet in the present condition. Note that this is the first demonstration for us with the availability of an electron beam current and laser power.

E. X-ray fluorescence measurement

As an application of the ERL-based LCS photon beam, we propose an advanced hybrid K-edge (KED)/x-ray fluorescence (XRF) densitometry (HKED) [34]. HKED is a nondestructive assay technique used for determining U and Pu concentrations in solutions [35]. In the conventional HKED system, an x-ray tube is used to produce bremsstrahlung radiation as an incident photon source. The bremsstrahlung radiation is characteristic of strong photon intensity with a continuous energy spectrum. However,

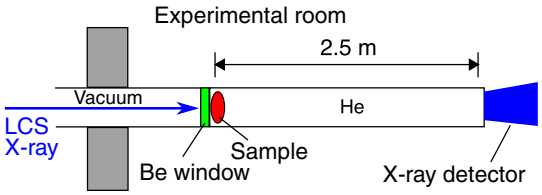

FIG. 26. Setup of the LCS x-ray imaging at the cERL.

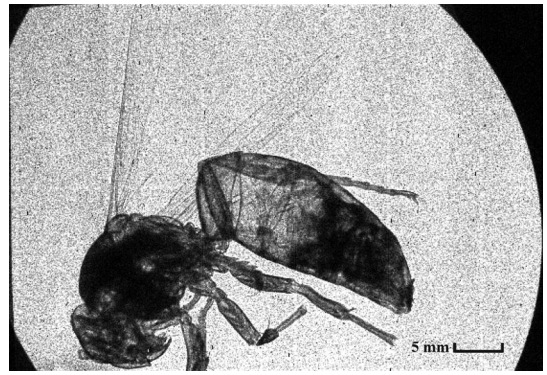

FIG. 27. LCS x-ray imaging of a hornet. The distance from the sample to the detector is 2.5 m for refraction contrast imaging.

broad energy distribution causes unnecessary background counts because of inelastic photon scattering, which affects the measurement precision. From the viewpoint of a Monte Carlo simulation study, we show that an accurate and precise HKED measurement is possible by using a narrow-bandwidth photon beam based on the ERL combined with the laser enhancement cavity [34]. When the energy width of the photon beam is low (less than a few %), efficient XRF measurements are possible by adjusting the photon beam energy just above the K absorption energy of the element.

To demonstrate the XRF measurement after selectively inducing K absorption, narrow-bandwidth photons from the cERL were used to bombard a 100 μm thick stainless-steel sheet. The emitted x-rays were measured using two low-energy, high-purity Ge detectors placed behind the target. Figures 29(a) and 29(b) show measured and simulated x-ray spectra, respectively. The measured spectrum was obtained by subtracting the backgrounds, which were measured independently without a laser. The simulated spectrum was obtained through a Monte Carlo simulation by using the EGS5 computer code [36]. In Fig. 29(a), characteristic K_α and/or K_β x-rays of chromium and manganese are clearly observed. The main constituents of stainless steel are iron, chromium, nickel, and manganese. As the energy of the LCS photon beam is 6.9 keV,

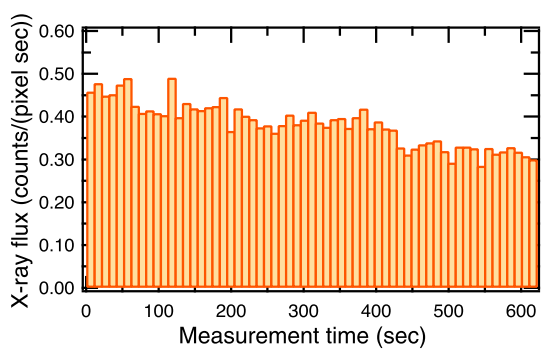

FIG. 28. LCS x-ray flux during image acquisition.

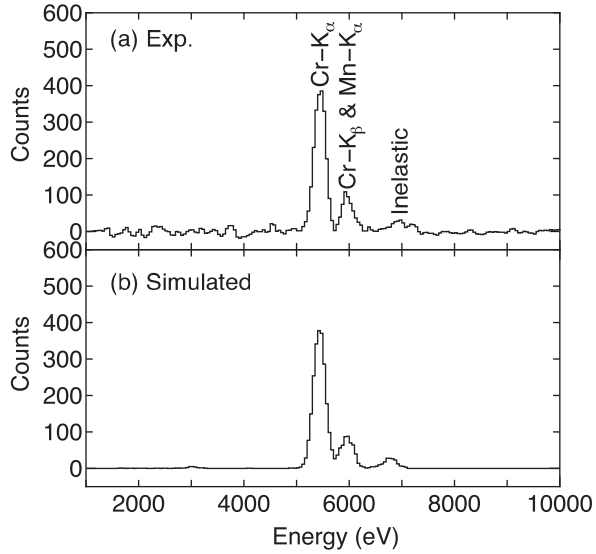

FIG. 29. X-ray spectra (a) measured with HP Ge detectors and (b) simulated with the EGS5 Monte Carlo computer code.

which is between the K absorption energies of manganese (6.539 keV) and iron (7.112 keV), only the K x-rays of chromium and manganese can be observed. The simulation determines the component ratios of chromium and manganese in the stainless-steel sheet as $18.0 \pm 0.5\%$ and $0.95 \pm 0.06\%$, respectively, which are in good agreement with the results (17.9% for chromium and 1.0% for manganese) obtained from wave length-dispersive x-ray spectroscopy (Rigaku, ZSX100e).

VI. DISCUSSION

A. Photon flux

We compare the measured and expected photon fluxes. The LCS x-rays were transported to the experimental room through the LCS beamline, as discussed in Sec. III. There are several factors that attenuate x-rays upstream of the detector. We quantitatively evaluate these factors. The combined transmittance of the two beryllium windows, which are installed at both ends of the LCS beamline, is 81%. The distance between the beryllium window and SDD is 12 cm. The transmittance of 7 keV x-rays in air is 80%. By considering the aperture of the SDD, the total flux at the IP is estimated to be $(2.6 \pm 0.1) \times 10^7$ photons/s from the measurement result of 1370 count/s at the SDD. In contrast, the expected photon flux is simulated to be 1.4×10^8 photons/s at the IP by CAIN. The experimental result is approximately 20% of the expectation. Following are the possible reasons for flux reduction: misalignment of the horizontal and longitudinal position of the laser beam at the IP, relatively large electron beam size at the IP, and pulse-width broadening of the laser beam inside the optical cavity. As we did not scan the horizontal position of the mover table when optimizing the spatial overlap, there might be some misalignment. However, even if 100 μm of misalignment remained, it only results in 6% luminosity reduction. If the focal point of the laser beam shows a positioning error of 3 mm in the longitudinal direction, it results in 10% luminosity reduction. The spot size at the IP was not measured directly, rather it was evaluated from the emittance and beta function. According to the width of the distribution on the vertical position scanning, the evaluated spot size is of the appropriate value. We believe that one of the most plausible reasons for this is the timing jitter of approximately 10 ps (rms) in phase-locking feedback. On calculating with a laser pulse width of 14 ps (rms including the timing jitter and pulse-width broadening), it results in 56% luminosity reduction. The photon flux obtained in the LCS experiment can be explained considering these errors. It is important to improve the accuracy of timing stability between the laser pulse and electron bunch to improve the luminosity.

B. Energy spectrum

A narrow bandwidth is an important feature of the ERL-based LCS photon source. We obtained a central energy of 6.95 ± 0.01 keV and an estimated energy width of 30 eV (rms) in the experiment. The energy bandwidth is calculated to be $\Delta E/E = 0.4\%$ (rms). By considering the 1% accuracy of the absolute energy of the electron beam, the expected LCS photon energy is 7.0 ± 0.1 keV. The measured x-ray energy is consistent with that of the calculation.

We calculated the LCS spectrum through CAIN simulation with the parameter of the LCS experiment and the energy spread of the electron beam set as 0.1% (rms). The calculation result shows that the central energy of the LCS photons is 6.96 keV, and the energy width is 14 eV (rms). The measured energy width of the LCS photon is approximately 2 times that obtained from the simulation.

A possible explanation is the different detection angle values. The angle of the electron beam path was aligned with an accuracy of 0.2 and 0.1 mrad for the horizontal and vertical directions, respectively. These values correspond to a detector position error of 3 and 2 mm for the horizontal and vertical positions, respectively. Assuming a positioning error of 1.5 mm in the horizontal and vertical directions, the calculated central energy and energy width were 6.84 keV and 28 eV, respectively. Figure 30 shows the calculated energy spectra at the detector. This shows that the energy bandwidth is sensitive to the detection angle. Therefore, it is important to properly align the electron beam axis along the detector for narrow-bandwidth LCS photons.

C. Source size

The source size is an important parameter for x-ray imaging applications. The spot size of the laser beam at the IP, $\sigma_L = 30$ μm, can be further reduced by changing the distance between the concave mirrors, as shown in Fig. 9.

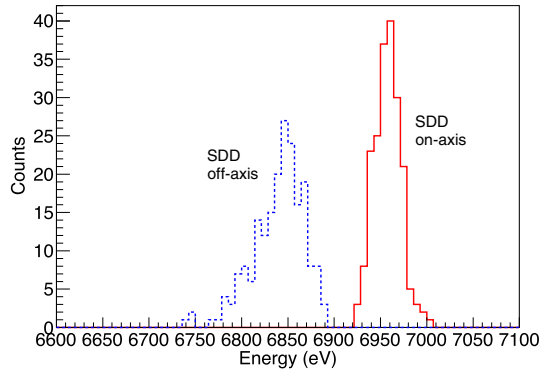

FIG. 30. Calculated energy spectra of the LCS photons at the detector. The solid line shows a spectrum with a perfectly aligned detector and the dotted line is for a detector having position error of 1.5 mm in the horizontal and vertical directions.

By precisely tuning the distance with an accuracy of 0.1 mm or better, the spot size can reach approximately 10 μm (rms) in the horizontal direction. However, the vertical spot size can reach only 30 μm because of astigmatism, which can be compensated for by introducing adaptive optics in the cavity mirrors [37,38]. This scheme can realize the small and round laser profile at the IP. However, the focusing of the horizontal spot size is not effective for luminosity with a crossing angle in the horizontal plane.

The spot size on mirrors increase with decreasing spot size at the IP. Therefore, it is necessary to consider diffraction loss at the mirrors. When the rms spot size at the IP is 10 μm, the spot size on mirrors is 1.7 mm with the geometry of our cavity. By assuming an effective diameter of 20 mm (80% of 25.4 mm), the spot size of 10 μm is acceptable because the effective diameter corresponds to a radius of 6-σ of the laser beam on the mirrors.

D. Future prospects

We describe the future prospects of the LCS photon source at the cERL developed through the improvement of the accelerator and laser system. The cERL is designed to achieve 10 mA electron beam current. Moreover, it achieved 1 mA beam operation after this LCS experiment [39]. To reach 10 mA, some hardware modification are required. However, the amount of the beam losses in the 1 mA operation indicates that the 10 mA operation is acceptable with the existing radiation shield. The enhancement factor of the optical cavity can be improved up to 1300 by improving the feedback system. For improving cavity-locking stability, in addition to reducing vibration and acoustic noise, widening the feedback bandwidth for a fast response is essential. Our present feedback system is restricted by response speed of the piezo actuator inside the laser oscillator. The fast response feedback is achieved by controlling the laser frequency electrically. By adding an electro-optic modulator (EOM) inside the laser oscillator [40] or an acousto-optic modulator (AOM) frequency shifter in the transport line [41], it is possible to realize a feedback response faster than 100 kHz. In combination with a 100 W-class mode-locked fiber laser, an average stored power higher than 100 kW can be expected. A high average power fiber chirped-pulse amplification (CPA) system has already been developed [42]. It can produce an average power of 100 W-class and has been successfully stored in the optical cavity. Note that the control of cavity mirror deformation due to a high average power will be necessary in this case. It is possible to reduce the influence of the cavity deformation by using mirror substrates of low coefficient of thermal expansion or by increasing the laser spot size on the mirror [43]. Furthermore, a crossing angle is one of the factors influencing the luminosity. The dependence of a crossing angle varies with the pulse width of the electron and laser beam. The luminosity with a crossing angle of 18° is approximately 30% of that for a head-on collision with the injected laser pulse width of 5.65 ps (rms). A crossing angle of approximately 6° is practically the minimum value because of the mechanical limitation of the beam duct and cavity mirror. In this case, the luminosity is approximately 70% of that for a head-on collision. Even if the crossing angle is 18°, luminosity reduction can be suppressed by using the small pulse width of the electron and laser beam.

Furthermore, the source size and precision during phase locking should be improved for efficient laser-beam collision. A total increase of photon flux by a factor of approximately 10^4 can be expected in the near future at the cERL. The LCS photon source can then be used for practical applications especially those that utilize features such as narrow bandwidth and energy tunability.

VII. CONCLUSION

We performed LCS photon generation at cERL. To our knowledge, this is the first experimental demonstration of ERL-based LCS by using a laser enhancement cavity. We obtained LCS photons of 6.95 ± 0.01 keV, and the photon flux at the IP was evaluated to be $(2.6 \pm 0.1) \times 10^7$ photons/s with an average beam current of 58 μA and an average laser power of 10 kW. The energy bandwidth was evaluated to be 0.4% (rms) with an opening angle of 0.14 mrad. The properties of LCS photons obtained in the experiment, such as photon flux, central energy, and energy width, can be explained by considering the electron and laser beam parameters. We also applied the LCS source to x-ray imaging and XRF analysis as demonstration experiments with narrow-band x-rays from a small spot size. The LCS technologies demonstrated in our experiment are applicable for a high-average-current electron beam and a high-power laser beam, and we plan to conduct an experiment at the cERL with a 10 mA beam current

and a 100 kW laser power to generate LCS photons with a flux greater than 10^{11} photons/s.

ACKNOWLEDGMENTS

We appreciate the cERL members for their support on the beam operation. We would also thank the people of Rigaku for their support on the x-ray imaging experiment. This work was supported by Photon and Quantum Basic Research Coordinated Development Program from the Ministry of Education, Culture, Sports, Science and Technology, Japan and by a Government (MEXT) Subsidy for Strengthening Nuclear Security.

[1] G. A. Krafft and G. Priebe, Compton sources of electromagnetic radiation, Rev. Accl. Sci. Tech. **03**, 147 (2010).

[2] K. Achterhold, M. Bech, S. Schleede, G. Potdevin, R. Ruth, R. Loewen, and F. Pfeiffer, Monochromatic computed tomography with a compact laser-driven X-ray source, Sci. Rep. **3**, 1313 (2013).

[3] R. Kuroda, H. Toyokawa, M. Yasumoto, H. Ikeura-Sekiguchi, M. Koike, K. Yamada, T. Yanagida, T. Nakajyo, F Sakai, and K. Mori, Quasi-monochromatic hard X-ray source via laser Compton scattering and its application, Nucl. Instrum. Methods Phys. Res., Sect. A **637**, S183 (2011).

[4] H. R. Weller, M. W. Ahmed, H. Gao, W. Tornow, Y. K. Wu, M. Gai, and R. Miskimen, Research opportunities at the upgraded HIγS facility, Prog. Part. Nucl. Phys. **62**, 257 (2009).

[5] R. Hajima *et al.*, Application of Laser Compton Scattered gamma-ray beams to nondestructive detection and assay of nuclear material, Eur. Phys. J. Spec. Top. **223**, 1229 (2014).

[6] T. Omori, M. Fukuda, T. Hirose, Y. Kurihara, R. Kuroda, M. Nomura, A. Ohashi, T. Okugi, K. Sakaue, T. Saito, J. Urakawa, M. Washio, and I. Yamazaki, Efficient Propagation of Polarization from Laser Photons to Positrons through Compton Scattering and Electron-Positron Pair Creation, Phys. Rev. Lett. **96**, 114801 (2006).

[7] M. Fujiwara, Hadron and nuclear physics with inverse compton gamma-rays at SPring-8, Prog. Part. Nucl. Phys. **50**, 487 (2003).

[8] S. F. Naeem, K Chouffani, and D. P. Wells, X-ray Fluorescence (XRF) Assay Using Laser Compton Scattered (LCS) X-rays, AIP Conf. Proc. **1099**, 843 (2009).

[9] R. Loewen, SLAC Report No. 632, 2003.

[10] A. Bacci *et al.*, Electron Linac design to drive bright Compton back-scattering gamma-ray sources, J. Appl. Phys. **113**, 194508 (2013).

[11] D. J. Gibson, F. Albert, S. G. Anderson, S. M. Betts, M. J. Messerly, H. H. Phan, V. A. Semenov, M. Y. Shverdin, A. M. Tremaine, F. V. Hartemann, C. W. Siders, D. P. McNabb, and C. P. J. Barty, Design and operation of a tunable MeV-level Compton-scattering-based γ-ray source, Phys. Rev. ST Accel. Beams **13**, 070703 (2010).

[12] F. Albert, S. G. Anderson, D. J. Gibson, C. A. Hagmann, M. S. Johnson, M. Messerly, V. Semenov, M. Y. Shverdin, B. Rusnak, A. M. Tremaine, F. V. Hartemann, C. W. Siders, D. P. McNabb, and C. P. J. Barty, Characterization and applications of a tunable, laser-based, MeV-class Compton-scattering γ-ray source, Phys. Rev. ST Accel. Beams **13**, 070704 (2010).

[13] F. Albert, S. G. Anderson, D. J. Gibson, R. A. Marsh, S. S. Wu, C. W. Siders, C. P. J. Barty, and F. V. Hartemann, Design of narrow-band Compton scattering sources for nuclear resonance fluorescence, Phys. Rev. ST Accel. Beams **14**, 050703 (2011).

[14] Y. Du, L. Yan, J. Hua, Q. Du, Z. Zhang, R. Li, H. Qian, W. Huang, H. Chen, and C. Tang, Generation of first hard X-ray pulse at Tsinghua Thomson Scattering X-ray Source, Rev. Sci. Instrum. **84**, 053301 (2013).

[15] A. Jochmann, A. Irman, U. Lehnert, J. P. Couperus, M. Kuntzsch, S. Trotsenko, A. Wagner, A. D. Debus, H.-P. Schlenvoigt, U. Helbig, S. Bock, K. W. D. Ledingham, T. E. Cowan, R. Sauerbrey, and U. Schramm, Operation of a picosecond narrow-bandwidth Laser–Thomson-backscattering X-ray source, Nucl. Instrum. Methods Phys. Res., Sect. B **309**, 214 (2013).

[16] C. Vaccarezza *et al.*, The SPARC_LAB Thomson source, Nucl. Instrum. Methods Phys. Res., Sect. A **829**, 237 (2016).

[17] I. Chaikovska and A. Variola, Equilibrium energy spread and emittance in a Compton ring: An alternative approach, Phys. Rev. ST Accel. Beams **17**, 044004 (2014).

[18] R. Hajima, Energy Recovery Linacs for Light Sources, Rev. Accl. Sci. Tech. **03**, 121 (2010).

[19] R. Hajima, M. Sawamura, E. Cenni, Y. Iwashita, H. Tongu, T. Kubo, and T. Saeki, Development of superconducting spoke cavities for laser compton scattered X-ray sources, in *Proceedings of the 2015 Particle Accelerator Conference, Richmond, VA, 2015* (JACOW, Richmond, 2015), p. 2902.

[20] R. Hajima, N. Kikuzawa, N. Nishimori, T. Hayakawa, T. Shizuma, K. Kawase, M. Kando, E. Minehara, H. Toyokawa, and H. Ohgaki, Detection of radioactive isotopes by using laser Compton scattered γ-ray beams, Nucl. Instrum. Methods Phys. Res., Sect. A **608**, S57 (2009).

[21] V. Petrillo, A. Bacci, R. B. A. Zinati, I. Chaikovska, C. Curatolo, M. Ferrario, C. Maroli, C. Ronsivalle, A. R. Rossi, L. Serafini, P. Tomassini, C. Vaccarezza, and A. Variola, Photon flux and spectrum of γ-rays Compton sources, Nucl. Instrum. Methods Phys. Res., Sect. A **693**, 109 (2012).

[22] P. Chen, G. Horton-Smith, T. Ohgaki, A. W. Weidemann, and K. Yokoya, CAIN: Conglomérat d'ABEL et d'Interactions Non-linéaires, Nucl. Instrum. Methods Phys. Res., Sect. A **355**, 107 (1995).

[23] N. Nishimori, R. Nagai, S. Matsuba, R. Hajima, M. Yamamoto, T. Miyajima, Y. Honda, H. Iijima, M. Kuriki, and M. Kuwahara, Generation of a 500-keV electron beam from a high voltage photoemission gun, Appl. Phys. Lett. **102**, 234103 (2013).

[24] E. Kako *et al.*, High power tests of injector cryomodule for compact-ERL, in *Proceedings of the 2013 Particle Accelerator Conference, Shanghai, China, 2013* (JACOW, Shanghai, 2013), p. 2340.

[25] K. Umemori, K. Enami, T. Furuya, H. Sakai, M. Satoh, K. Shinoe, M. Sawamura, and E. Cenni, Status of Main Linac cryomodule development for compact ERL project, in

Proceedings of the 3rd International Particle Accelerator Conference, New Orleans, LA, 2012 (IEEE, Piscataway, NJ, 2012), p. 67.

[26] T. Miyajima, Y. Honda, R. Takai, T. Obina, M. Shimada, K. Harada, M. Yamamoto, K. Umemori, H. Sakai, T. Miura, F. Qiu, N. Nakamura, S. Sakanaka, N. Nishimori, R. Nagai, R. Hajima, and D. Lee, Status of higher bunch charge operation in compact ERL, in *Proceedings of the 2015 Particle Accelerator Conference, Richmond, VA, 2015* (JACOW, Richmond, 2015), p. 1583.

[27] S. Sakanaka *et al.*, Recent progress and operational status of the compact ERL at KEK, in *Proceedings of the 2015 Particle Accelerator Conference, Richmond, VA, 2015* (JACOW, Richmond, 2015), p. 1359.

[28] I. V. Bazarov and C. K. Sinclair, Multivariate optimization of a high brightness dc gun photoinjector, Phys. Rev. ST Accel. Beams **8**, 034202 (2005).

[29] R. Hajima and R. Nagai, Multiparameter optimization of an ERL injector, Nucl. Instrum. Methods Phys. Res., Sect. A **557**, 103 (2006).

[30] F. Zomer, Y. Fedala, N. Pavloff, V. Soskov, and A. Variola, Polarization induced instabilities in external four-mirror Fabry-Perot cavities, Appl. Opt. **48**, 6651 (2009).

[31] F. A. Jenkins and H. E. White, *Fundamentals of Optics* (McGraw-Hill, New York, 1976).

[32] T. W. Hänsch and B. Couillaud, Laser frequency stabilization by polarization spectroscopy of a reflecting reference cavity, Opt. Commun. **35**, 441 (1980).

[33] X. Liu, K. Cassou, R. Chiche, K. Dupraz, P. Favier, R. Flaminio, Y. Honda, W. H. Huang, A. Martens, C. Michel, L. Pinard, B. Sassolas, V. Soskov, C. X. Tang, and F. Zomer, Laser frequency stabilization using folded cavity and mirror reflectivity tuning, Opt. Commun. **369**, 84 (2016).

[34] T. Shizuma, R. Hajima, T. Hayakawa, M. Fujiwara, T. Sonoda, and M. Seya, Proposal for an advanced hybrid K-edge/XRF densitometry (HKED) using a monochromatic photon beam from laser Compton scattering, Nucl. Instrum. Methods Phys. Res., Sect. A **654**, 597 (2011).

[35] H. Ottmar and H. Eberle, Kernforschungszentrum Karlsruhe GmbH, Institut fur Kernphysik, Report No. 4590, 1991.

[36] H. Hirayama, Y. Namito, A. F. Bielajew, S. J. Wilderman, and W. R. Nelson, Report No. SLAC-R-730, 2005.

[37] H. Shimizu, A. Aryshev, Y. Higashi, Y. Honda, and J. Urakawa, Development of a 4-mirror optical cavity for an inverse Compton scattering experiment in the STF, Nucl. Instrum. Methods Phys. Res., Sect. A **745**, 63 (2014).

[38] H. Carstens, S. Holzberger, J. Kaster, J. Weitenberg, V. Pervak, A. Apolonski, E. Fill, F. Krausz, and I. Pupeza, Large-mode enhancement cavities, Opt. Express **21**, 11606 (2013).

[39] T. Obina *et al.*, Recent developments and operational status of the compact ERL at KEK, in *Proceedings of the 7th International Particle Accelerator Conference (IPAC'16), Busan, Korea, 2016* (JACOW, Busan, 2016), p. 1835.

[40] D. D. Hudson, K. W. Holman, R. J. Jones, S. T. Cundiff, J. Ye, and D. J. Jones, Mode-locked fiber laser frequency-controlled with an intracavity electro-optic modulator, Opt. Lett. **30**, 2948 (2005).

[41] A. Börzsönyi, R. Chiche, E. Cormier, R. Flaminio, P. Jojart, C. Michel, K. Osvay, L. Pinard, V. Soskov, A. Variola, and F. Zomer, External cavity enhancement of picosecond pulses with 28,000 cavity finesse, Appl. Opt. **52**, 8376 (2013).

[42] C. Jocher, T. Eidam, S. Hädrich, J. Limpert, and A. Tünnermann, Sub 25 fs pulses from solid-core nonlinear compression stage at 250 W of average power, Opt. Lett. **37**, 4407 (2012).

[43] H. Carstens, N. Lilienfein, S. Holzberger, C. Jocher, T. Eidam, J. Limpert, A. Tünnermann, J. Weitenberg, D. C. Yost, A. Alghamdi, Z. Alahmed, A. Azzeer, A. Apolonski, E. Fill, F. Krausz, and I. Pupeza, Megawatt-scale average-power ultrashort pulses in an enhancement cavity, Opt. Lett. **39**, 2595 (2014).